

LETTER TO THE EDITOR

The spine of the swan: A *Herschel*^{*} study of the DR21 ridge and filaments in Cygnus X

M. Hennemann¹, F. Motte¹, N. Schneider¹, P. Didelon¹, T. Hill¹, D. Arzoumanian¹, S. Bontemps^{2,3}, T. Csengeri⁴, Ph. André¹, V. Konyves¹, F. Louvet¹, A. Marston⁵, A. Men'shchikov¹, V. Minier¹, Q. Nguyen Luong^{6,1}, P. Palmeirim¹, N. Peretto¹, M. Sauvage¹, A. Zavagno⁷, L. D. Anderson⁸, J.-Ph. Bernard⁹, J. Di Francesco¹⁰, D. Elia¹¹, J. Z. Li¹², P. G. Martin⁶, S. Molinari¹¹, S. Pezzuto¹¹, D. Russeil⁷, K. L. J. Rygl¹¹, E. Schisano¹¹, L. Spinoglio¹¹, T. Sousbie¹³, D. Ward-Thompson¹⁴, G. J. White^{15,16}

(Affiliations can be found after the references)

Received 2012; accepted 2012

ABSTRACT

In order to characterise the cloud structures responsible for the formation of high-mass stars, we present *Herschel* observations of the DR21 environment. Maps of the column density and dust temperature unveil the structure of the DR21 ridge and several connected filaments. The ridge has column densities larger than 10^{23} cm^{-2} over a region of 2.3 pc^2 . It shows substructured column density profiles and branching into two major filaments in the north. The masses in the studied filaments range between 130 and $1400 M_{\odot}$ whereas the mass in the ridge is $15000 M_{\odot}$. The accretion of these filaments onto the DR21 ridge, suggested by a previous molecular line study, could provide a continuous mass inflow to the ridge. In contrast to the striations seen in e.g., the Taurus region, these filaments are gravitationally unstable and form cores and protostars. These cores formed in the filaments potentially fall into the ridge. Both inflow and collisions of cores could be important to drive the observed high-mass star formation. The evolutionary gradient of star formation running from DR21 in the south to the northern branching is traced by decreasing dust temperature. This evolution and the ridge structure can be explained by two main filamentary components of the ridge that merged first in the south.

Key words. ISM: individual objects (DR21, DR21(OH)) – ISM: general – ISM: structure – dust, extinction – Stars: formation

1. Introduction

The properties of dense structures in interstellar molecular clouds, e.g., the density and temperature distribution, chemical composition, and dynamics, are expected to determine the detailed outcome of the star formation process that varies between an isolated low-mass star and an OB star cluster. While previous observations have shown that clouds are filamentary (e.g., Bally et al. 1987), recent *Herschel* studies have revealed the ubiquity (e.g., Miville-Deschênes et al. 2010; Henning et al. 2010) and key importance of filaments for star formation. Notably, gravitationally unstable filaments are found to fragment into cores (André et al. 2010), and filaments generally show narrow central widths of about 0.1 pc (Arzoumanian et al. 2011). Resulting self-gravitating cores with sizes of 0.01–0.1 pc and masses up to $10 M_{\odot}$ are best candidates to form low- to possibly intermediate-mass stars (see reviews by Di Francesco et al. 2007; Ward-Thompson et al. 2007).

It is an important question which cloud structures lead to the formation of high-mass stars ($\geq 10 M_{\odot}$) almost exclusively found in stellar clusters or associations (see review by Zinnecker & Yorke 2007). The *Herschel* imaging survey of OB Young Stellar objects (HOBYS, Motte et al. 2010) observes massive molecular cloud complexes within 3 kpc distance to probe the cloud environment of OB star-forming cores, their statistical evolu-

tion, and the effects of feedback on parental clouds. Studying the Vela C region, Hill et al. (2011) suggested that “ridges”, i.e., massive, gravitationally unstable filamentary structures of high column density ($N_{\text{H}_2} > 10^{23} \text{ cm}^{-2}$) that dominate their environment could be preferential sites of high-mass star formation (cf. Nguyen Luong et al. 2011). The ridge in Vela C shows a complex substructure that could result from stellar feedback (Minier et al. 2012). Further, intersecting filaments appear to mark sites of stellar cluster formation in the Rosette cloud (Schneider et al. 2012).

This study focusses on the DR21 ridge (also called DR21 filament), the densest and most massive cloud structure in the Cygnus X region (Schneider et al. 2006; Motte et al. 2007; Roy et al. 2011) at a distance of 1.4 kpc (Rygl et al. 2012). It hosts the embedded HII region DR21 (e.g., Roelfsema et al. 1989), the maser source DR21(OH), and massive protostars (Bontemps et al. 2010). Schneider et al. (2010) analysed molecular line emission and identified three “sub-filaments” F1–F3 that connect to the ridge. Velocity gradients suggest that material is transported along them towards the ridge, and in the case of F3 a bend and possible direct connection to the DR21(OH) clump is traced (cf. Csengeri et al. 2011). This behaviour supports the scenario that sustained accretion of inflowing material plays a role in building up massive clumps and cores and setting the stage for high-mass star formation, as suggested by numerical simulations (e.g., Balsara et al. 2001; Banerjee et al. 2006; Smith et al. 2011). Here we exploit the unprecedented sensitivity of *Herschel* far-infrared and submillimeter continuum imaging to trace the detailed column density structure in this region.

^{*} *Herschel* is an ESA space observatory with science instruments provided by European-led Principal Investigator consortia and with important participation from NASA (Pilbratt et al. 2010).

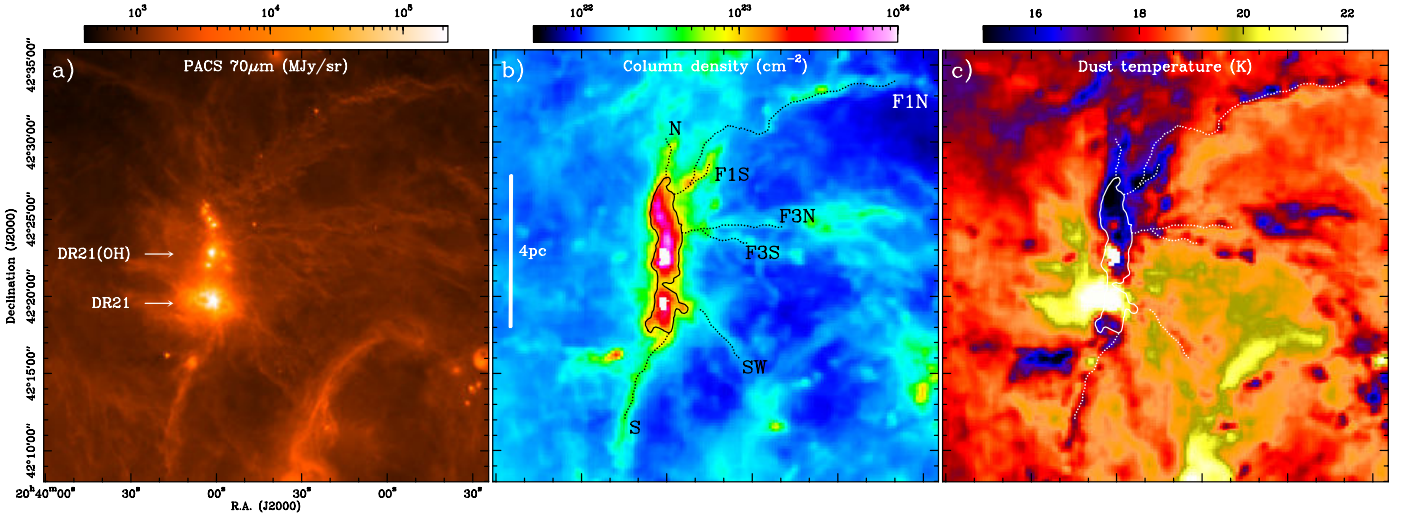


Fig. 1: *Herschel* maps of the DR21 environment showing a) 70 μm emission, b) column density, and c) dust temperature. The DR21 ridge is delimited roughly by the $N_{\text{H}_2} = 10^{23} \text{ cm}^{-2}$ contour plotted in panels b) and c). The filaments selected using *DisPerSE* (see Section 3) are named and marked with dots along their crests in b) and c).

2. *Herschel* observations and data reduction

Cygnus X North was observed in the parallel scan map mode with PACS (Poglitsch et al. 2010) and SPIRE (Griffin et al. 2010) on Dec 18, 2010. To diminish scanning artifacts, two nearly perpendicular coverages of $2.8 \times 2.8^\circ$ were obtained in five photometric bands at 70, 160, 250, 350, and 500 μm with a scan speed of $20''/\text{sec}$. The data were reduced using the *Herschel Interactive Processing Environment* and the *Scanamorphos* software (Roussel 2012, for creating PACS maps).

The 70 μm map traces in particular heated dust towards star-forming sites (Fig. 1 a). To quantitatively estimate the distribution of the cold dust which generally represents most of the dust mass, we created maps of column density N_{H_2} and dust temperature T_d in the way described in Hill et al. (2011, 2012), including offsets to recover the absolute intensity level following Bernard et al. (2010). Computed from the 160, 250, and 350 μm bands, the maps provide an angular resolution of $25''$ (0.17 pc at 1.4 kpc). They have undefined values for pixel groups towards DR21, DR21(OH) (white pixels in Fig. 1 b), and W75N (see Fig. B.1) due to saturation at 250 and 350 μm .

3. The DR21 filaments

Shown in Fig. 1 a, compact 70 μm sources that are protostar candidates cluster along the DR21 ridge oriented north-south, with the most prominent peak being DR21 itself. Supposedly lying at the same distance, they show a strong northward decrease in luminosity. Many filamentary streamers from the ridge to e.g., the north-west and west, are present, most of which were also detected in the mid-infrared with *Spitzer* (Marston et al. 2004; Hora et al. 2009). They mainly correspond to low column density structures (Fig. 1 b), but several filaments are prominent. The extent of the DR21 ridge can be roughly defined by the $N_{\text{H}_2} = 10^{23} \text{ cm}^{-2}$ contour enclosing an area of 2.3 pc^2 . Notably, the “sub-filaments” of Schneider et al. (2010) labeled F1 and F3 are recovered, both being resolved into nearly parallel northern and southern components that join close to the ridge. The northern part of the DR21 ridge shows two extensions in column density (“rabbit ears”) to the north and north-west (F1) which coincide with the coldest regions where the dust temperature drops

as low as 14 K (Fig. 1 c). The filaments are visible in the dust temperature map as structures of lower central temperature relative to the background of $\sim 19 \text{ K}$. The background column density level is $\sim 10^{22} \text{ cm}^{-2}$ with a standard deviation of $\sim 10^{21} \text{ cm}^{-2}$ mainly due to cirrus structure.

In the first step to characterise the DR21 filaments, we applied the *DisPerSE* software (Sousbie 2011) on the column density map to identify the filament crests (cf. Arzoumanian et al. 2011; Hill et al. 2011) using a persistence threshold of $3 \times 10^{21} \text{ cm}^{-2}$. Unlike for these works, possible line-of-sight confusion needed to be addressed in our analysis due to the low-density foreground cloud Cygnus Rift and the close-by W75N cloud component (e.g., Schneider et al. 2006). Also the strong DR21 outflow (e.g., Richardson et al. 1986; White et al. 2010) is avoided. Subsequent studies will analyse the combined column density, temperature, and kinematical data for a larger region, but here we conservatively limited this study to filaments that (1) have main velocities in ^{13}CO coherent with the ridge and no strong secondary velocity components^a, and (2) have crest column densities above $1.5 \times 10^{22} \text{ cm}^{-2}$; the resulting selection is shown in Fig. 1. At positions along their crests spaced by half the beam FWHM we extracted perpendicular column density profiles extending over 2.5 pc in each direction, wide enough so that the outer profiles are sufficiently flat and trace the background. For background column densities, we adopted the profile minima that were median-smoothed over 2.5 beam FWHM to lower the influence of neighbouring structures.

Crest column density and dust temperature are anti-correlated as anticipated for all filaments with the possible exception of SW (Fig. 2 a, b). Contrary to the others, the latter shows slightly decreasing central temperature outward from the DR21 ridge. This filament also shows the weakest outward column density decline. In general, lower temperatures are expected for structures of higher column density due to the increased shielding from the interstellar radiation field. However, the SW filament is running towards the warmer area around DR21 (Fig. 1 a, c) and possibly into the outflow cavity. Its in-

^a We used the Schneider et al. (2010) FCRAO ^{13}CO (1-0) data and excluded filament segments showing additional velocity components above the 20% level of the primary peak.

Table 1: Average properties of the DR21 filaments and ridge

	S	SW	F3S	F3N	F1S	F1N	N	Ridge
Length (pc)	2.6	1.6	1.3	2.7	1.3	6.9	1.1	4.1
Mean crest column density ^a (10^{22} cm^{-2})	4.4	1.2	1.6	2.1	7.7	1.9	4.8	41.6
Integration radius (pc)	0.58	0.41	0.24	0.24	0.48	0.39	0.49	1.15
Total mass (M_{\odot})	1350	210	130	400	960	1210	610	15210
Mean line mass (M_{\odot}/pc)	500	120	100	140	700	170	520	3670
Weighted mean central width ^b (pc)	0.28 ± 0.07	0.31 ± 0.07	0.27 ± 0.08	0.32 ± 0.11	0.26 ± 0.07	0.33 ± 0.16	0.34 ± 0.17	0.34 ± 0.12

Notes. ^(a) Background-subtracted column density. ^(b) The fit error in width σ_w was used for weighting data points with $1/\sigma_w^2$.

verted density-temperature relation could thus be an effect of heating by DR21.

The perpendicular filament column density profiles generally show a flattened central part and non-Gaussian, roughly power-law wings. To examine the central width we performed a weighted fit of a Gaussian curve plus a constant level (cf. Arzoumanian et al. 2011). As weights a Gaussian curve with 0.17 pc FWHM was used to ensure the reproduction of the central flattening. The central width of each profile was derived as deconvolved fitted Gaussian FWHM. The weighted mean values of the profile central widths lie between 0.26 and 0.34 pc (Table 1). These values are beyond the range around the typical ~ 0.1 pc found by Arzoumanian et al. (2011), probably only partially caused by the lower spatial resolution. However, no correlation between central width and crest column density is present, neither for profiles nor for the mean values. Better statistics in the high-column density regime is needed to clarify a possible dependency.

To constrain the masses of the filaments we estimated an outer radius for each profile integration. A threshold per profile was derived by building the cumulative integral over radial distance from the crest and determining the first minimum of its derivative. For each filament we adopted its median threshold as integration radius, ranging from 0.24 to 0.58 pc (Table 1).

In theory, the thermal stability of filaments is to first order determined by the critical mass per unit length^b (e.g., Inutsuka & Miyama 1992). Observations indicate that this is a proxy for the general stability (André et al. 2010). Most filament segments are thermally supercritical (Fig. 2c). The outer segments (beyond 1 pc) of the SW, F3N, and F3S filaments are only supercritical to within a factor of 3, and the longest, F1N filament shows a marginally subcritical segment. For thermally supercritical filaments, fragmentation and local spherical collapse occur faster than global collapse in the absence of other stabilising mechanisms (Pon et al. 2011; Toalá et al. 2012). In this case we thus expect the DR21 filaments to form cores and protostars. The S filament shows several local maxima of crest column density separated by about 1 pc (Fig. 2a). Less regular and prominent, several peaks are also seen for the other filaments. At $70 \mu\text{m}$ there is one extended source towards the S filament (Figs. 1a, A.1a). Compact emission from protostar candidates is present towards the junction point of F3S and F3N, and towards the F1N and N filaments. The $250 \mu\text{m}$ map shows additional compact starless/prestellar core candidates towards all filaments, one of them identified as dense core by Motte et al. (2007) (see Apps. A, B). This confirms that core and star formation is ongoing within the thermally supercritical filaments.

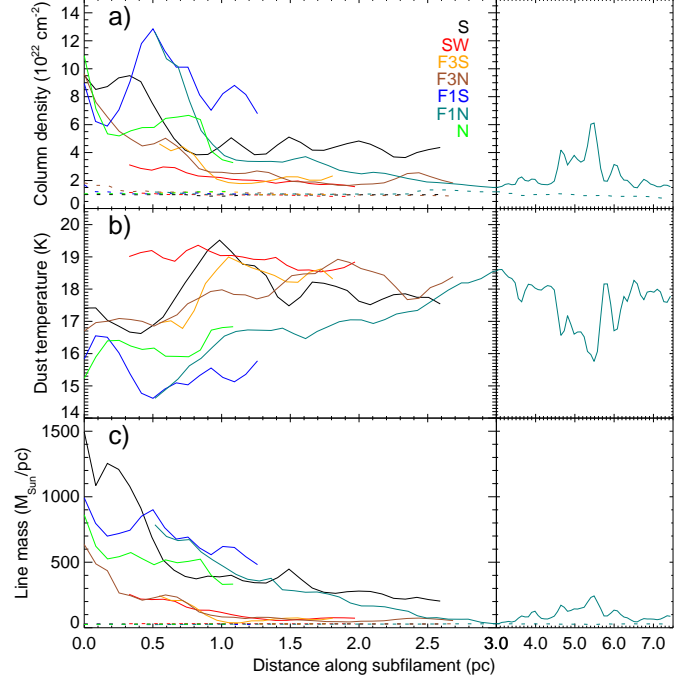


Fig. 2: DR21 filament properties over distance along their crest from the DR21 ridge. The distance scale is compressed beyond 3 pc. a) Crest column density (not background-subtracted), dashed curves show the background column density, b) Crest dust temperature, c) Mass per unit length, dashed lines gives the critical value.

4. The DR21 ridge – an intersection of filaments

The DR21 ridge hosts 22 dense cores and $\sim 1/4$ of the massive ones in the Motte et al. (2007) sample of the whole cloud complex, and thus represents the probable region to host the most massive forming star cluster in Cygnus X. We used their MAMBO 1.2 mm map to interpolate the missing pixels in the column density map and derived the mean ridge properties using a crest of 4 pc length following its main peaks (Fig. 3a, Table 1). If it were regarded as an individual filament, it would be highly unstable, in accord with the global collapse signature observed by Schneider et al. (2010) and the dense core detections (Fig. 3a).

The chain of cores dominates the structure of the ridge except between DR21 and DR21(OH), where a crest column density dip is present (location c in Fig. 3). Less clear than the northern branching, a possible additional filamentary extension coinciding with a core branches off to the south-east at the southern end of the ridge (at the very bottom of Fig. 3a). As illustrated in Fig. 3b for location b, corresponding to the dense core N40, the column density profile of the ridge generally shows

^b $M_{\text{line}}^{\text{crit}} = 2c_s^2/G$ with the isothermal sound speed $c_s = \sqrt{RT_d/\mu_{\text{H}_2}}$ and T_d at the crest position, resulting in $M_{\text{line}}^{\text{crit}} \approx 30 M_{\odot}/\text{pc}$.

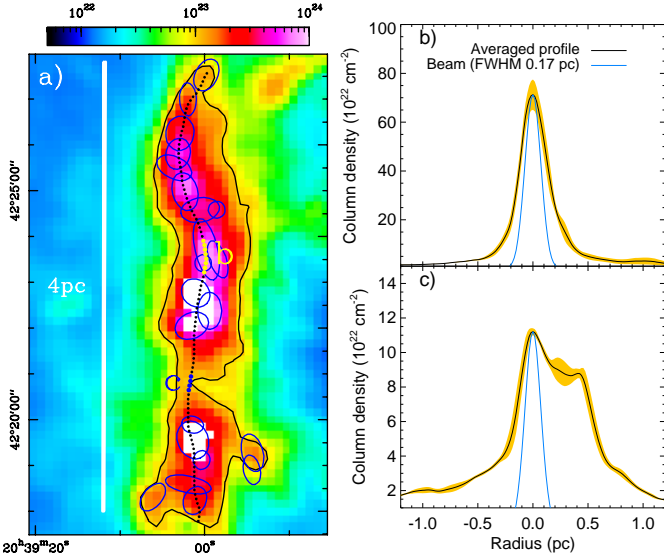


Fig. 3: a) Column density map (in cm^{-2}) of the DR21 ridge with the crest as black dots and the black $\text{N}_{\text{H}_2} = 10^{23} \text{ cm}^{-2}$ contour. Note that white pixels are undefined due to saturation. Blue ellipses give the position and extent (FWHM = semiaxes) of the Motte et al. (2007) dense cores. b), c) Radial column density profiles towards the crest locations b and c marked in yellow/blue in a). The radial profiles are averaged over the marked crest dots. The yellow areas show the $\pm 1 \sigma$ ranges.

narrow peaks and smoothly decreasing wings towards the cores. However, the profile towards location c shows at least one additional peak of $9 \times 10^{22} \text{ cm}^{-2}$ at 0.4 pc (Fig. 3 c), indicating that there the ridge consists of more than one individual filament. Considered together with the branching of the northern ridge into the “rabbit ears” (the F1 and N filaments) and the possible southern branching, this finding suggests that the DR21 ridge is a complex intersection of several individual filaments. The dominating filament along the crest shows a central width of $\sim 0.34 \text{ pc}$, not significantly larger than the central widths of the filaments (Table 1).

5. Star formation in the DR21 ridge

Schneider et al. (2010) present velocity gradients that suggest accretion of the filaments onto the DR21 ridge. Dust temperature dips are seen towards the filament-ridge connections (Fig. 2 b), indicating that inflowing material has cooled at these locations. At present, the total mass in the selected filaments is about 1/3 of the ridge mass. It thus appears that the mass assembly process of the DR21 ridge is in a late stage, possibly driven by the gravitational potential of the ridge itself, and specifically the build-up of massive cores in the DR21/DR21(OH) clumps could have been supported by continuous accretion from the S/SW and F3S/F3N filaments, respectively. The filaments are for the most part gravitationally unstable and forming cores and protostars, in contrast to the striations and “sub-filaments” in Taurus (Goldsmith et al. 2008, Palmeirim et al. in prep.) or Aquila (André et al. 2010). The high masses of the cores in the ridge could thus not only be due to the filament flows, but also due to the merging with fragment cores of the filaments that form dense, small-scale convergent flows. For DR21(OH), Csengeri et al. (2011) showed possible fragmentation of the inflowing material. High-mass star for-

mation involving a core merger process was also suggested by observations of NGC 2264-C (Peretto et al. 2006).

The *Herschel* observations emphasize the evolutionary gradient along the ridge: Beyond DR21, the $70 \mu\text{m}$ luminosity of protostars strongly decreases northward, and the dust temperature shows lowest temperatures towards the northern part. The substructure of the DR21 ridge suggests that it was formed by the merging of individual narrow, intersecting filaments. The pronounced elongation and branching into filaments F1 and N with the highest mass per unit length indicate that the major components may be roughly parallel filaments oriented north-south. At present, the merging could have advanced furthest in the southern part and less in the north, where the two components appear separated. Extrapolating this scenario, we expect that the northern filaments will lead to the assembly of one or more further massive clumps. This study suggests that high-mass star-forming ridges could be second-generation cloud structures formed via dynamical merging of gravitationally unstable filaments.

References

- André, P., Men'shchikov, A., Bontemps, S., et al. 2010, *A&A*, 518, L102
 Arzoumanian, D., André, P., Didelon, P., et al. 2011, *A&A*, 529, L6
 Bally, J., Lanber, W. D., Stark, A. A., & Wilson, R. W. 1987, *ApJ*, 312, L45
 Balsara, D., Ward-Thompson, D., & Crutcher, R. M. 2001, *MNRAS*, 327, 715
 Banerjee, R., Pudritz, R. E., & Anderson, D. W. 2006, *MNRAS*, 373, 1091
 Bernard, J.-P., Paradis, D., Marshall, D. J., et al. 2010, *A&A*, 518, L88
 Bontemps, S., Motte, F., Csengeri, T., & Schneider, N. 2010, *A&A*, 524, A18
 Csengeri, T., Bontemps, S., Schneider, N., et al. 2011, *ApJ*, 740, L5
 Di Francesco, J., Evans, II, N. J., Caselli, P., et al. 2007, in *Protostars and Planets V*, ed. B. Reipurth, D. Jewitt, & K. Keil, 17–32
 Goldsmith, P. F., Heyer, M., Narayanan, G., et al. 2008, *ApJ*, 680, 428
 Griffin, M. J., Abergel, A., Abreu, A., et al. 2010, *A&A*, 518, L3
 Henning, T., Linz, H., Krause, O., et al. 2010, *A&A*, 518, L95
 Hill, T., Motte, F., Didelon, P., et al. 2011, *A&A*, 533, A94
 Hill, T., Motte, F., Didelon, P., et al. 2012, accepted by *A&A* (arXiv:1204.6317)
 Hora, J. L., Bontemps, S., Megeath, S. T., et al. 2009, *BAAS*, 41, 498
 Inutsuka, S.-I. & Miyama, S. M. 1992, *ApJ*, 388, 392
 Marston, A. P., Reach, W. T., Noriega-Crespo, A., et al. 2004, *ApJS*, 154, 333
 Minier, V., Tremblin, P., Hill, T., et al. 2012, submitted to *A&A*
 Miville-Deschênes, M.-A., Martin, P. G., Abergel, A., et al. 2010, *A&A*, 518, L104
 Motte, F., Bontemps, S., Schilke, P., et al. 2007, *A&A*, 476, 1243
 Motte, F., Zavagno, A., Bontemps, S., et al. 2010, *A&A*, 518, L77
 Nguyen Luong, Q., Motte, F., Hennemann, M., et al. 2011, *A&A*, 535, A76
 Peretto, N., André, P., & Belloche, A. 2006, *A&A*, 445, 979
 Pilbratt, G. L., Riedinger, J. R., Passvogel, T., et al. 2010, *A&A*, 518, L1
 Poglitsch, A., Waelkens, C., Geis, N., et al. 2010, *A&A*, 518, L2
 Pon, A., Johnstone, D., & Heitsch, F. 2011, *ApJ*, 740, 88
 Richardson, K. J., White, G. J., Phillips, J. P., & Avery, L. W. 1986, *MNRAS*, 219, 167
 Roelfsema, P. R., Goss, W. M., & Geballe, T. R. 1989, *A&A*, 222, 247
 Roussel, H. 2012, submitted to *A&A* (arXiv:1205.2576)
 Roy, A., Ade, P. A. R., Bock, J. J., et al. 2011, *ApJ*, 727, 114
 Rygl, K. L. J., Brunthaler, A., Sanna, A., et al. 2012, *A&A*, 539, A79
 Schneider, N., Bontemps, S., Simon, R., et al. 2006, *A&A*, 458, 855
 Schneider, N., Csengeri, T., Bontemps, S., et al. 2010, *A&A*, 520, A49
 Schneider, N., Csengeri, T., Hennemann, M., et al. 2012, *ArXiv e-prints*
 Smith, R. J., Glover, S. C. O., Bonnell, I. A., Clark, P. C., & Klessen, R. S. 2011, *MNRAS*, 411, 1354
 Soubie, T. 2011, *MNRAS*, 414, 350
 Toalá, J. A., Vázquez-Semadeni, E., & Gómez, G. C. 2012, *ApJ*, 744, 190
 Ward-Thompson, D., André, P., Crutcher, R., et al. 2007, in *Protostars and Planets V*, ed. B. Reipurth, D. Jewitt, & K. Keil, 33–46
 White, G. J., Abergel, A., Spencer, L., et al. 2010, *A&A*, 518, L114
 Zinnecker, H. & Yorke, H. W. 2007, *ARA&A*, 45, 481

Acknowledgements. SPIRE has been developed by a consortium of institutes led by Cardiff Univ. (UK) and including: Univ. Lethbridge (Canada); NAOC (China); CEA, LAM (France); IFSI, Univ. Padua (Italy); IAC (Spain);

Stockholm Observatory (Sweden); Imperial College London, RAL, UCL-MSSL, UKATC, Univ. Sussex (UK); and Caltech, JPL, NHSC, Univ. Colorado (USA). This development has been supported by national funding agencies: CSA (Canada); NAOC (China); CEA, CNES, CNRS (France); ASI (Italy); MCINN (Spain); SNSB (Sweden); STFC, UKSA (UK); and NASA (USA). PACS has been developed by a consortium of institutes led by MPE (Germany) and including UVIE (Austria); KU Leuven, CSL, IMEC (Belgium); CEA, LAM (France); MPIA (Germany); INAF-IFSI/OAA/OAP/OAT, LENS, SISSA (Italy); IAC (Spain). This development has been supported by the funding agencies BMVIT (Austria), ESA-PRODEX (Belgium), CEA/CNES (France), DLR (Germany), ASI/INAF (Italy), and CICYT/MCYT (Spain). This work was supported by the ANR (*Agence Nationale pour la Recherche*) project “PROBeS” (ANR-08-BLAN-0241).

Appendix A: The S and F1N filaments in detail

Figure A.1 shows a zoom on the S and F1N filaments. Several compact, more or less elongated cores are seen in the $250\mu\text{m}$ and column density map. The marked dense core N23 has an estimated mass of $13 M_{\odot}$.

-
- ¹ AIM Paris-Saclay, CEA/DSM/IRFU – CNRS/INSU – Université Paris Diderot, CEA Saclay, 91191 Gif-sur-Yvette cedex, France e-mail: martin.hennemann@cea.fr
 - ² Université de Bordeaux, LAB, UMR5804, F-33270 Floirac, France
 - ³ CNRS, LAB, UMR5804, F-33270 Floirac, France
 - ⁴ Max-Planck-Institut für Radioastronomie, Auf dem Hügel 69, 53121 Bonn, Germany
 - ⁵ Herschel Science Centre, ESAC, ESA, PO Box 78, Villanueva de la Cañada, 28691 Madrid, Spain
 - ⁶ Canadian Institute for Theoretical Astrophysics - CITA, University of Toronto, 60 St. George Street, Toronto, Ontario, M5S 3H8, Canada
 - ⁷ Laboratoire d’Astrophysique de Marseille, CNRS/INSU – Université de Provence, 13388 Marseille cedex 13, France
 - ⁸ Department of Physics, West Virginia University, Morgantown, WV 26506, USA
 - ⁹ Université de Toulouse, UPS, CESR, 9 avenue du colonel Roche, 31028 Toulouse Cedex 4, France; CNRS, UMR5187, 31028 Toulouse, France
 - ¹⁰ National Research Council of Canada, Herzberg Institute of Astrophysics, 5071 West Saanich Road, Victoria, BC V9E 2E7, Canada
 - ¹¹ Istituto di Astrofisica e Planetologia Spaziali - IAPS, Istituto Nazionale di Astrofisica - INAF, Via Fosso del Cavaliere 100, I-00133 Roma, Italy
 - ¹² National Astronomical Observatories, Chinese Academy of Sciences, A20 Datun Road, Chaoyang District, 100012 Beijing, China
 - ¹³ Institut d’Astrophysique de Paris, Université Pierre et Marie Curie (UPMC), CNRS (UMR 7095), 75014 Paris, France
 - ¹⁴ Jeremiah Horrocks Institute, University of Central Lancashire, PR1 2HE, UK
 - ¹⁵ Department of Physics & Astronomy, The Open University, Walton Hall, Milton Keynes MK7 6AA, UK
 - ¹⁶ Space Science & Technology Department, CCLRC Rutherford Appleton Laboratory, Chilton, Didcot, Oxfordshire OX11 0QX, UK

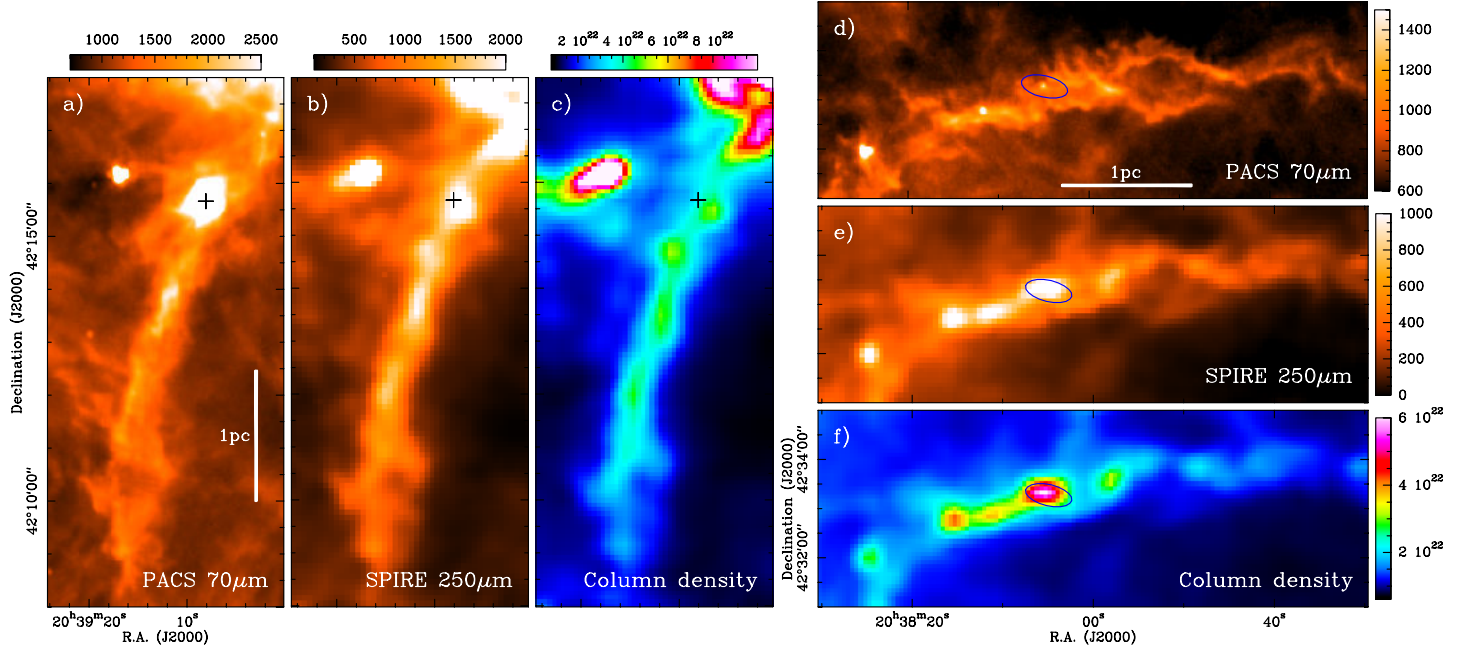


Fig. A.1: Detailed view of filament S (panels a, b, c) and F1N (d, e, f). The 70 and 250 μ m units are MJy/sr, column density unit is cm^{-2} . The black cross in panel a) indicates an extended 70 μ m source. The blue ellipse in panels d), e), f) gives the position and extent (FWHM = semiaxes) of the dense core N23 of Motte et al. (2007).

Appendix B: *Herschel* maps of DR21 and Cygnus X North

Figure B.1 shows the DR21 environment in the *Herschel* maps of the HOBYS Cygnus X North observations together with a RGB colour composite image.

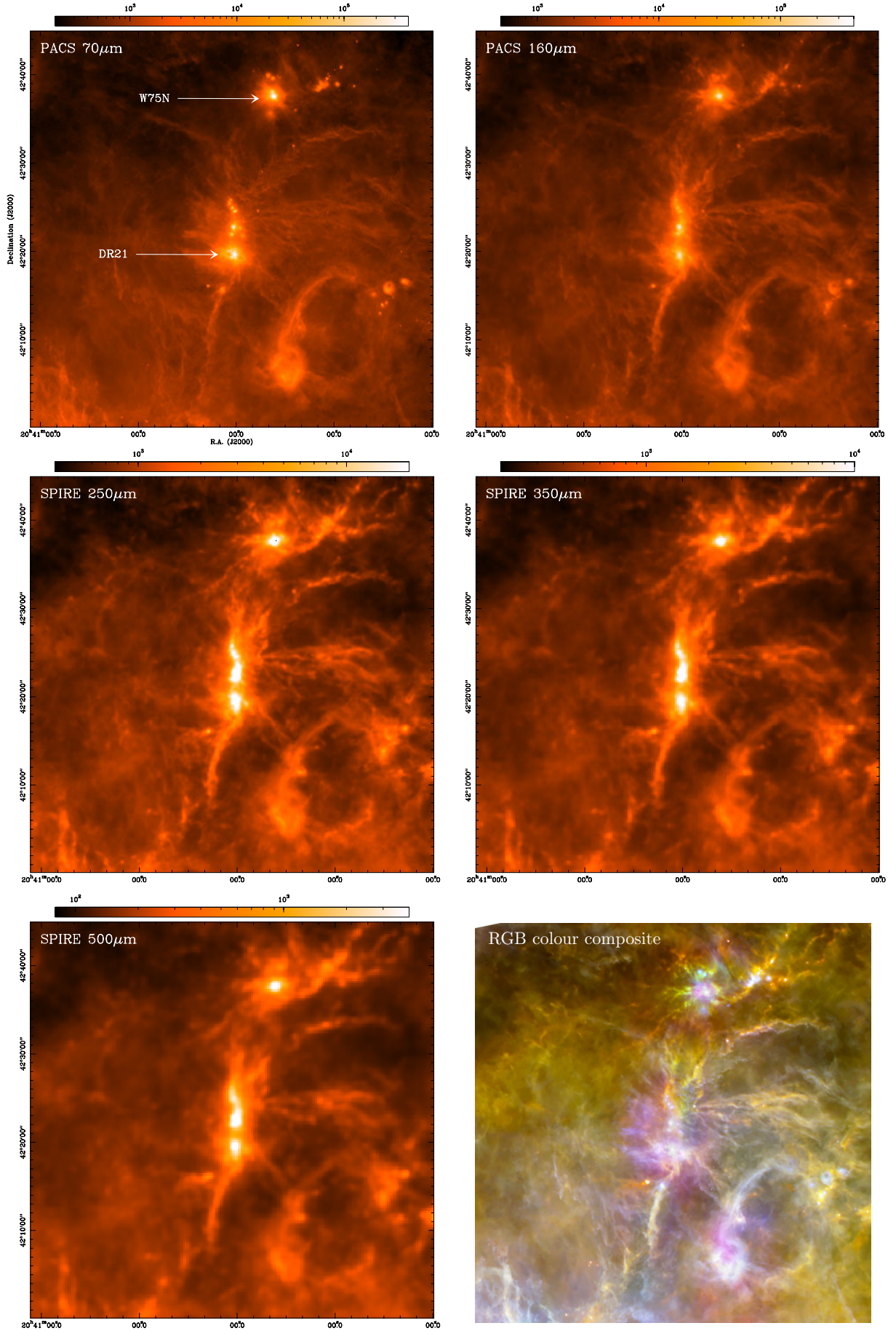


Fig. B.1: *Herschel* maps of the DR21 environment in Cygnus X North obtained by HOBYS. Map units are MJy/sr. The last panel shows a RGB colour composite image using the SPIRE 250 μm (red), PACS 160 μm (green), and PACS 70 μm (blue) maps.